Received: 27 May 2022 | Revised: 18 June 2022 | Accepted: 30 June 2022

DOI: 10.1049/mna2.12135

Micro & Nano Letters

The Institution of Engineering and Technology WILEY

LETTER

Hierarchical zinc oxide nanobrushes ultraviolet photodetector

Mohammad R. Alenezi[1,2] | **Abdullah M. Almeshal**[3] | **Abdullah NFNR. Alkhaledi**[4]

[1]Science Department, College of Basic Education, PAAET, Ardhya, Kuwait

[2]Nanoelectronics Center, Advanced Technology Institute, University of Surrey, Surrey, UK

[3]College of Technological Studies, PAAET, Shuwaikh, Kuwait

[4]Engineering, Cranfield University, Bedfordshire, UK

Correspondence
Mohammad R. Alenezi, Science Department, College of Basic Education, PAAET, Block 1 street 141 house 600, Alqayrawan 12064, Kuwait.
Email: mr.alenezi@paaet.edu.kw

Abstract

In order to synthesise hierarchical zinc oxide (ZnO) nanomaterials with a high surface-to-volume ratio, a well-controlled multistage hydrothermal method was developed. Hierarchical ZnO nanobrushes (ZNBs) built from initial mono-morphological nanomaterials, ZnO nanowires (ZNWs), and ZnO nanoplates (ZNPs) were developed using sequential nucleation and growth following a hydrothermal process. Hierarchical nanomaterials which are comprised of one-dimensional (1D) nanowire building blocks were obtained via a zinc ion source (zinc nitrate) during the second growth phase. In comparison to their first mono-morphological equivalents, the hierarchical nanomaterials which were grown showed improved ultraviolet (UV) detection, as well as improved sensitivity ($\sim 10^4$), an ultra-fast response time (235 ms), and a good recovery time (310 ms). Improvements to the response and recovery times were a result of distinct nanojunction barrier-dominated resistance. Moreover, the enhanced sensitivity of the ZNB photodetector (PD) was because of the reduced dimensionality and the ultrahigh surface-to-volume ratio. This work lays the groundwork for lower-cost, larger-scale, and lower-temperature production of high-performance nanostructured ZnO-based PDs on transparent and flexible substrates.

1 | INTRODUCTION

Due to the economic and industrial growth race between nations and the accelerated technological development, water and air pollution rates have crossed all red lines and have become an unprecedented danger not only to humanity but also to life as we know it on this planet. Therefore, researchers around the world today must unite their efforts to combat this threat with scientific research and find solutions to monitor and dismantle pollutants in new and more effective ways. Ultraviolet (UV) photodetection is an important method in environmental monitoring and disease diagnosis. Moreover, UV photodetectors (PDs) have been utilised in the military and commercial sectors for uses such as secure space communications, purification of water, and flame and missile plume detection [1–9]. In addition, because of the health risks related to overexposure to UV irradiation, UV PDs are required that exhibit a high sensitivity, a good detectability, a quick response and recovery, and a high responsivity. The UV PD material and structure are the most important factors in the photodetection process. The semiconductors such as TiO_2, SnO_2, and ZnO are widely used in the UV photodetection field because of their availability, low cost, low hazard, and effectiveness, which can be improved greatly by producing these materials at the nanoscale and with more efficient device structures [1–9].

Zinc oxide (ZnO) is a typical n-type semiconductor with a wide band gap (E_g = 3.26 eV) and large exciton binding energy (60 meV). ZnO has one of the widest ranges of nanomaterial morphologies and possesses many advantageous characteristics such as good thermal stability, low cost, biodegradability, and biocompatibility. Hence, they play important roles in many fields including optoelectronics, electronics, piezoelectronics, energy generation and storage, gas sensing, air and water purification, photocatalysis, and photodetection [9–15].

As previously reported, high-temperature synthesis methods are used for producing hierarchical ZnO nanomaterials, for example nanowires arrays[16], nanohelixes [17], nanopropellers [18], and tower-like nanocolumns [19]. Yet, high temperatures have numerous drawbacks and limitations, including impurities in the final product, a limited number of applicable substrates, the requirement for high temperatures (i.e. 500°C–1100°C), and the use of vacuum conditions. Therefore, because of the

This is an open access article under the terms of the Creative Commons Attribution License, which permits use, distribution and reproduction in any medium, provided the original work is properly cited.
© 2022 The Authors. *Micro & Nano Letters* published by John Wiley & Sons Ltd on behalf of The Institution of Engineering and Technology.

17500443, 2022, 12, Downloaded from https://ietresearch.onlinelibrary.wiley.com/doi/10.1049/mna2.12135 by Test, Wiley Online Library on [14/10/2022]. See the Terms and Conditions (https://onlinelibrary.wiley.com/terms-and-conditions) on Wiley Online Library for rules of use; OA articles are governed by the applicable Creative Commons License

limited economic possibility of larger-scale production using these techniques, there has been increased attention towards developing cost-effective and low-temperature solution phase methods so that these nanomaterials can be produced on a larger scale [20–22]. Although there are advantages of solution phase techniques in the growth mono-morphological nanomaterials, the use of techniques to create hierarchical architectures with rational control over the size and morphology remains a challenge. Because of their extraordinary chemical and physical properties, increased attention has been paid to the preparation of hierarchical structures based on one-dimensional (1D) or two-dimensional (2D) nanostructured building blocks [23–28]. In particular, these structures have already shown as applicable in the bottom-up production of high-performance devices [11–15, 23–28].

Keeping these systems in mind, we report the development of an elegant nucleation and growth strategy to synthesise various hierarchical ZnO nanobrushes (ZNBs) from mono-morphological nanomaterials. This two-step growth tactic permits step-by-step tuning and optimisation of the experimental conditions, as well as offering rational design and synthesis of controlled nanostructured architectures. The role played by structure and morphology of the prepared hierarchical ZnO nanomaterials in their performance as UV detectors is also investigated and compared with other grown nanomaterials.

2 | EXPERIMENT

In this study, every reagent was of analytical grade. Synthesising ZnO nanowires (ZNWs) was performed as detailed in the previous report [23]. Specifically, a seeded silicon (Si) substrate was put into a vial which contained a growth solution (15 ml) comprised of 25 to 50 mM zinc nitrate, 12.5 to 25 mM hexamethylenetetramine (HMTA), 0.35 to 0.45 M ammonium hydroxide, and 5 mM polyethyleneimine (PEI, end-capped, molecular weight 800 g/mol LS, Aldrich). Next, the vial was covered and put into an oven which had been heated to 90°C, and heating was continued for 24 h. Following this, the substrate was rinsed with deionised (DI) water and air-dried at 150°C for 30 min. Finally, the prepared ZNWs were suspended uniformly in DI water (20 ml) in an ultrasonic bath.

Preparation of the ZnO nanoplates (ZNPs) has been previously detailed [23]. In this case, a 15-ml vial of the growth solution which consisted of 100 mM zinc sulphate ($ZnSO_4$) and 100 mM HMTA was heated to 75°C for 3 h in an oven. Thorough filtering and washing of the grown nanomaterials was then performed using ethanol and distilled water, in sequence.

Subsequently, the ZNBs were synthesised with the prepared ZNWs and ZNPs as seeds in the second stage of growth. More specifically, a suspension of the initial ZNWs or ZNPs was combined with fresh growth solution, such as that used for initially growing ZNWs. The vial which contained the mixture was maintained at 90°C for 5 h, and then the grown products were thoroughly washed with ethanol and distilled water in sequence, then dried at 80°C.

Analysis of the as-prepared products' crystal structures was performed using powder X-ray diffraction (XRD) using a PANalytical X-pert diffractometer with Cu Kα radiation. The morphologies and crystal structures were observed with a scanning electron microscopy (SEM) using a Philips XL-20 scanning electron microscope at 10 kV. Electron diffraction measurements and scanning transmission electron microscopy (STEM) were conducted using a Hitachi-HD2300A microscope, operating at 200 kV. Preparation of the STEM samples was performed by placing a droplet of the diluted nanomaterial suspension in ethanol onto a carbon film-coated copper grid.

The fabricated device's electrical aspects were measured using a probe station connected to a Keithley 4200 semiconductor analyser. The source of excitation for the UV detection was a monochromatic UV lamp (UVGL-55 Hand-Lamp from UVP-LLC) with a 50 $\mu W/cm^2$ intensity at a wavelength of 365 nm. All measurements were carried out at a bias voltage of 2 V.

3 | RESULTS AND DISCUSSION

3.1 | Morphology and structure

Figures 1a and 1b illustrate the low- and high-magnification side-view SEM images of a uniform and well-aligned ZNW array (ZNWA), respectively, while Figures 1c and 1d show the corresponding low- and high-magnification top-view SEM images, respectively. The SEM images explicitly reveal the compact nature and excellent uniformity of the ZNWs. Figures 1e and 1f show low- and high-magnification SEM images of a single ZNW which connect to two gold electrodes, respectively, while Figure 1g shows the resultant selected areas of electron diffraction (SAED) ZNWs pattern. The ZNWs were found to be single crystals which grew in the [0001] direction, and their side surfaces are comprised of non-polar $\{10\bar{1}0\}$ planes. Figure 1h illustrates the XRD pattern of the as-grown ZNWs, whereby the observed peaks provide confirmation that the ZNWs are highly crystalline and can be represented by the hexagonal wurtzite-type ZnO structure (JCPDS No. 36-1451).

Figures 2a–d show the SEM images corresponding to the SAED pattern, STEM image, and XRD pattern of a single ZNP, respectively. The majority of the exposed facets in the ZNP morphology are polar [0001] facets, whilst the XRD pattern and the STEM image show that the resulting ZNPs are highly crystalline and can be represented by the hexagonal wurtzite-type ZnO structure (JCPDS No. 36-1451).

No impurities peaks were detected, which indicate that the zinc salt precursors have been completely transformed into ZnO in the hydrothermal growth reaction. Yet, the (002) XRD diffraction intensity of the polar facet of the hydrothermally produced ZNWs is relatively low in comparison with the usual observation of high-intensity ZnO (002) peak in XRD analysis of ZNWAs in the literature. The high-intensity ZnO (002) peak represents the good alignment of the ZNWs growing in the *c* direction. The ZNWs in this work showed a lower intensity (002) peak because they are relatively long with low density leading to a poor alignment. Additionally, these ZNWs can

17500443, 2022, 12, Downloaded from https://ietresearch.onlinelibrary.wiley.com/doi/10.1049/mna2.12135 by Test, Wiley Online Library on [14/10/2022]. See the Terms and Conditions (https://onlinelibrary.wiley.com/terms-and-conditions) on Wiley Online Library for rules of use; OA articles are governed by the applicable Creative Commons License

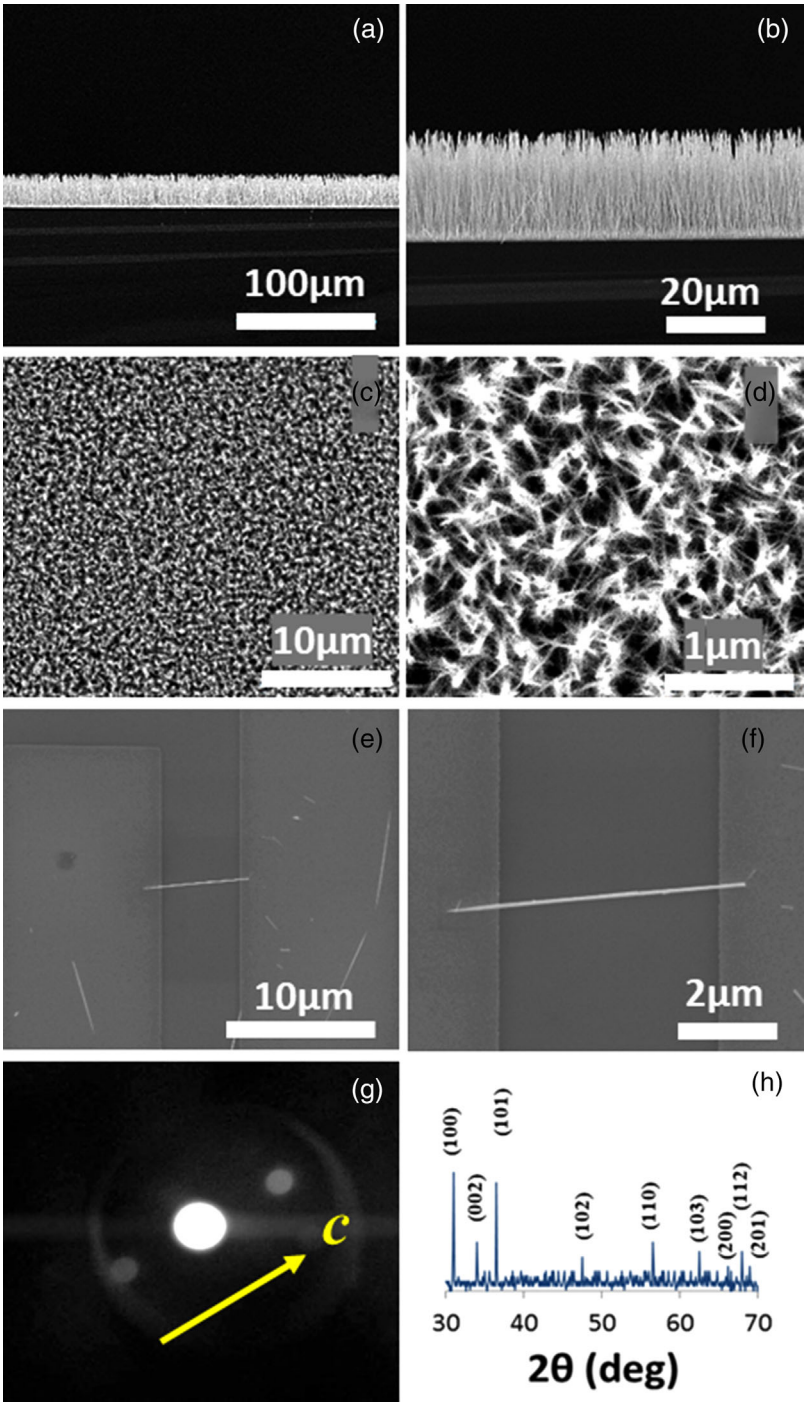


FIGURE 1 (a) Low-magnification side-view SEM image, (b) high-magnification side-view SEM image, (c) low-magnification top-view SEM image, and (d) high-magnification top-view SEM image of an array of ZNWs. (e) Low-magnification SEM image and (f) high-magnification SEM image of a single ZNW. (g) The corresponding SAED pattern for the ZNWs and (h) the XRD pattern of the ZNWs. SAED, selected areas of electron diffraction; SEM, scanning electron microscopy; XRD, X-ray diffraction; ZNW, zinc oxide nanowires.

easily break and lay on the substrate. On the other hand, the high diffraction peak for the ZNPs indicates that there are more nanostructures with their *c* direction normal to the substrate than for the ZNWs.

Hydrothermally grown ZnO nanomaterials typically adopt a 1D form as a result of the high growth rate of crystals in the [0001] direction [23]. We have previously found that different counter-ions of zinc can often alter the final morphological structure of the grown nanocrystals [24]. For ZNPs, the 2D structure is because of anisotropic growth, whereby the growth sideways is more rapid than in the axial direction. The zinc terminated (0001) facet which is positively charged prefers to absorb counter-anions (e.g. SO_4^{2-}) into the growth system rather than hydroxyl anions. Consequently, the $[Zn(OH)_4]^{2-}$ species required for growth cannot attach to the (0001) surface; therefore, the nanocrystal must grow sideways rather than the expected intrinsic anisotropic growth along the (0001) direction [23, 24].

Thus, in the current system, the two mono-morphological ZnO nanomaterials produced in the initial growth phase, namely the ZNWs and the ZNPs, were used as seeds to produce the desired ZNBs in the second growth phase. Figures 3a

17500443, 2022, 12, Downloaded from https://ietresearch.onlinelibrary.wiley.com/doi/10.1049/nna2.12135 by Test, Wiley Online Library on [14/10/2022]. See the Terms and Conditions (https://onlinelibrary.wiley.com/terms-and-conditions) on Wiley Online Library for rules of use; OA articles are governed by the applicable Creative Commons License

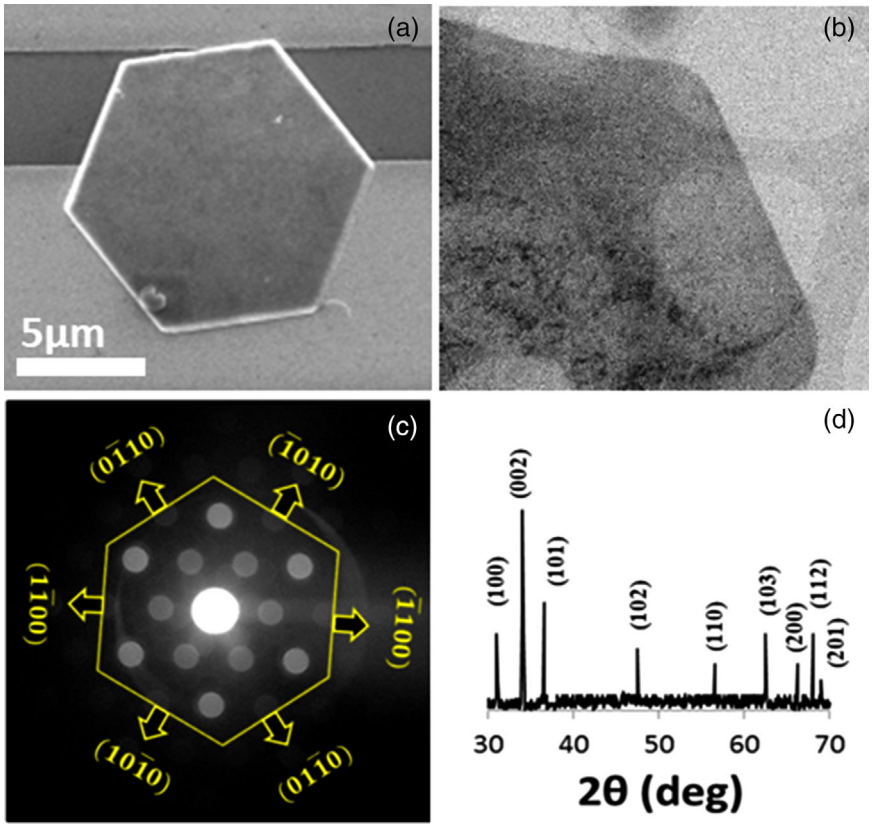


FIGURE 2 (a) An SEM image, (b) the corresponding SAED pattern, (c) the STEM image, and (d) the XRD pattern of the ZNPs. STEM, scanning transmission electron microscopy; ZNP, zinc oxide nanoplates.

to d, which provide the SEM images of a single ZNB grown from a ZNW, show that the secondary ZNWs will grow in the *c* direction on the six sides of the initial ZNW to form a six-fold symmetry. In addition, Figure 3e shows a high-magnification image of the secondary ZNWs. It should be noted that in the hydrothermal synthesis of ZNWs, heterogeneous nucleation is preferable to homogenous nucleation as the interfacial energy between the crystal nuclei and the substrate is less than that between the crystal nuclei and the solution [24]. Consequently, during the second growth phase the secondary ZNWs prefer growing on the surfaces of the mono-morphological ZnO nanomaterials. We also examined using ZNPs as seeds to produce ZNBs. The low- and high-magnification top-view SEM images of a single ZNB are shown in Figures 3f and 3g, while Figure 3h provides a tilted view SEM image of a single ZNB showing the secondary ZNWs that grow on both faces of the initial ZNP. These SEM images show the density and uniformity of the secondary ZNWs. They also indicate that the secondary ZNWs grew along the *c*-axis with their side surfaces being non-polar planes. In addition, SEM analysis reveals that all of the prepared secondary ZNWs have a flat top, corresponding to a polar (0001) facet.

Using our hydrothermal synthesis technique, we controlled and manipulated the ZnO nanomaterial morphology by tuning the growth parameters, including the growth temperature, the growth concentration, the zinc counter-ions, the growth time, and the PEI concentration. For example, the density of the secondary ZNWs was controlled by varying the growth solution concentration in the second growth phase. Specifically, Figures 3a to d show the ZNBs that were produced using a growth concentration of 12.5 mM in the second growth phase. Conversely, lowering the concentration to 5 mM produced ZNBs with a low secondary ZNW density, as shown in Figure 4a. However, increasing the growth concentration to 25 mM in the second growth phase significantly enhanced the density of the secondary ZNWs, as shown in Figures 4b to e. It was also found that at high growth concentrations, the secondary ZNWs lost their six-fold symmetry. Subsequently, the length and diameter of the secondary ZNWs were controlled by variations in the growth time and the PEI concentration, respectively. Consequently, our well-controlled hydrothermal technique allowed high surface-to-volume ratio ZNBs to be prepared. Additionally, Figures 4f and 4g show the SEM images of the ZNBs grown from the initial ZNPs with a high secondary ZNW density (see Figure 4h for a high-magnification SEM image of the secondary ZNWs). SEM analysis clearly demonstrates that ZNBs have a higher surface-to-volume ratio than their mono-morphological nanomaterial counterparts; therefore, they have the potential for superior performances as UV PDs.

After confirming that the ZNBs had been successfully produced, the materials were used to prepare nanostructured ZnO PDs. Likewise, two different ZnO nanostructured PDs were produced based on ZNWAs and single ZNWs to be compared with the ZNB-based PDs. The photo response aspects of the ZNWA-, single ZNW-, and ZNB-based PDs are shown in Figures 5a to 5c, respectively, which show that the photosensitivity of the ZNWA-based PD, which is the ratio of the

17500443, 2022, 12, Downloaded from https://ietresearch.onlinelibrary.wiley.com/doi/10.1049/nna2.12135 by Test, Wiley Online Library on [14/10/2022]. See the Terms and Conditions (https://onlinelibrary.wiley.com/terms-and-conditions) on Wiley Online Library for rules of use; OA articles are governed by the applicable Creative Commons License

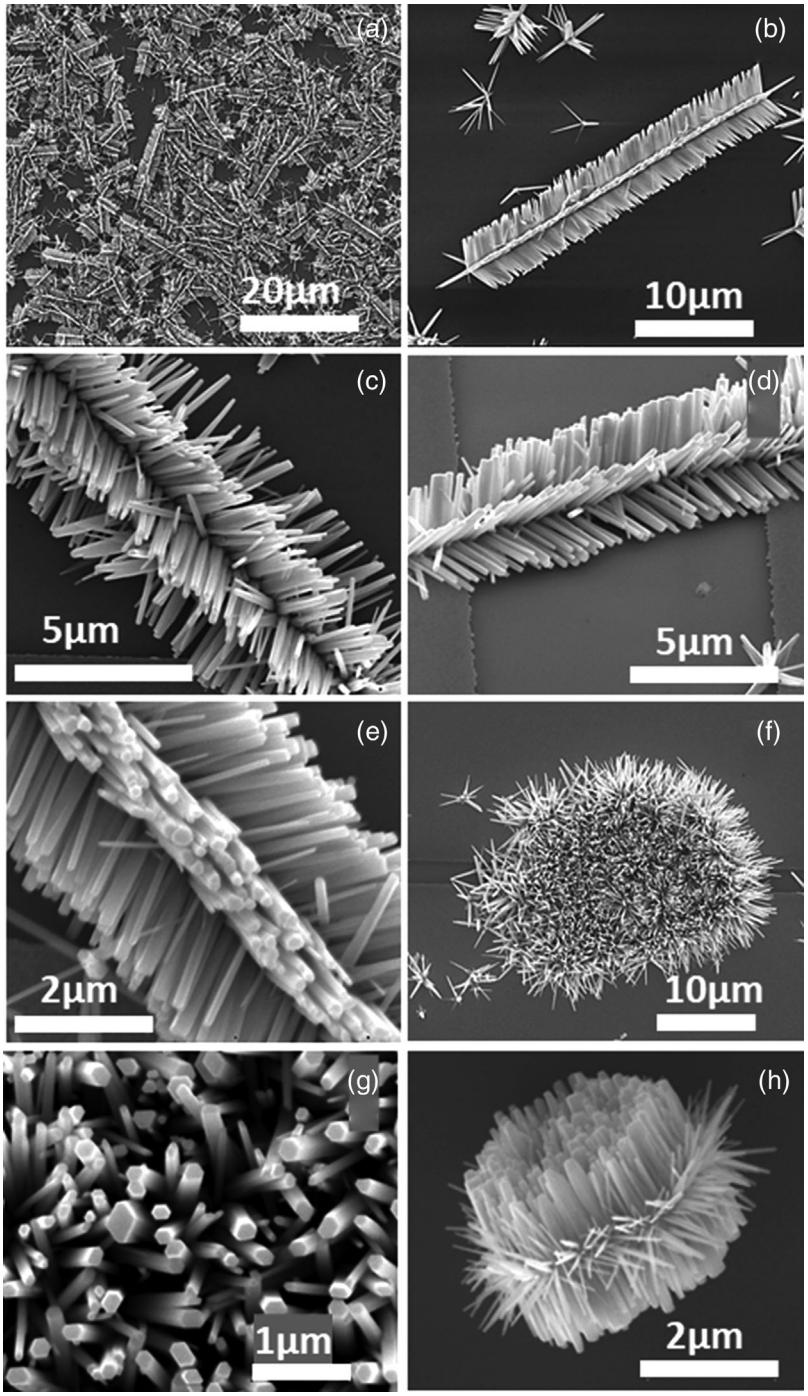


FIGURE 3 (a) SEM image showing numerous ZNBs grown from the initial ZNWs. (b) SEM image of a single ZNB. (c) SEM image of a ZNB connecting two gold electrodes. (d) High-magnification SEM image of a single ZNB. (e) High-magnification SEM image of the secondary ZNWs. (f) Top-view SEM image of a ZNB grown from an initial ZNP. (g) High-magnification top-view SEM image of the ZNB. (h) Tilted-view SEM image of a ZNB. ZNB, zinc oxide nanobrushes.

photocurrent I_{ph} to the dark current I_d, was ~30. In addition, the response and recovery times were 42 and 55 s, respectively. Several UV PDs using this type of device structure were tested, and often the response and recovery times were extended to several minutes. It should be noted that the conduction channel in the ZNWA-based PD is the seed layer beneath the ZNWs which connects the two gold electrodes (i.e. a polycrystalline film of ~300 to 400 nm thickness). As shown in Figure 5, the photo response of the ZNWA-based PD has high stability and repeatability, although it has low photosensitivity, and the response and recovery times are longer. Conversely, the single ZNW-based PD exhibited photosensitivity of ~1200, as well as response and recovery times of 11 and 15 s, respectively. These significant improvements in photosensitivity and response and recovery times were the result of a reduction in the dimensionality of the single ZNWs compared to ZNWAs. Moreover, the photo response facets of the ZNB-based PD exhibited enhanced photosensitivity of ~10^4, which are three orders of magnitude greater than the ZNWA-based PD and 8.3-times that of the ZNW-based PD. Figure 5d shows that the response and recovery times of the ZNBs PD were 235 and 310 ms, respectively, demonstrating that the ZNB-based

17500443, 2022, 12, Downloaded from https://ietresearch.onlinelibrary.wiley.com/doi/10.1049/mna2.12135 by Test, Wiley Online Library on [14/10/2022]. See the Terms and Conditions (https://onlinelibrary.wiley.com/terms-and-conditions) on Wiley Online Library for rules of use; OA articles are governed by the applicable Creative Commons License

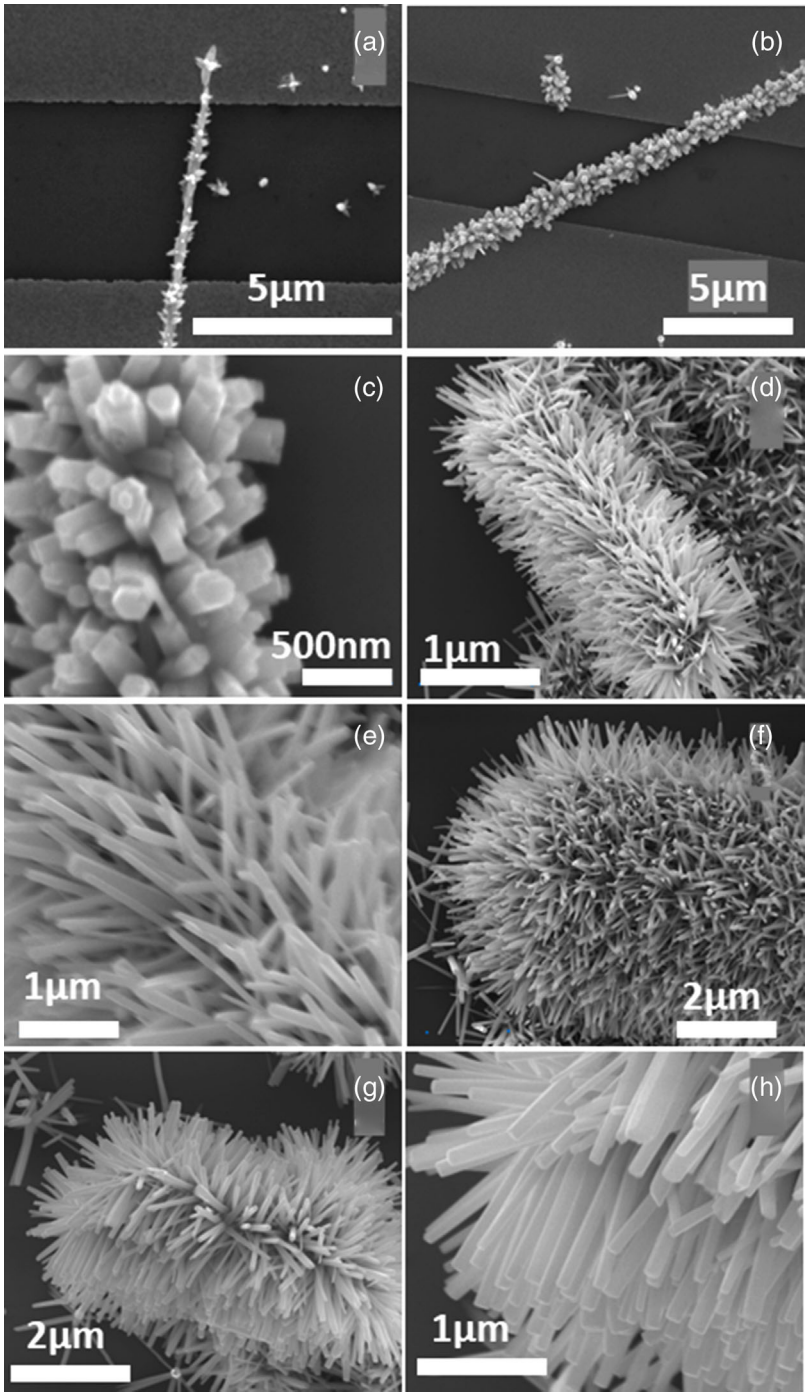


FIGURE 4 (a) SEM image of a ZNB bearing a low density of secondary ZNWs. (b) SEM image of a ZNB bearing a high density of secondary ZNWs. (c) High-magnification SEM image of the high-density secondary ZNWs. (d) SEM images of a ZNB bearing a high density of long secondary ZNWs. (e) High-magnification SEM image of the secondary ZNWs. (f, g) SEM images of ZNBs grown from initial ZNPs with a high secondary ZNW density. (h) A high magnification SEM image of the highly dense secondary ZNWs

PD was 191 times faster than the ZNWA-based PD, and 47 times faster than the ZNW-based PD. The superior photosensitivity of the ZNB-based PD in comparison to other prepared devices results from the lower dimensions; its high surface-to-volume ratio, and the enhanced efficiency of its device structure, is the result of nanojunctions forming between the initial and secondary ZNWs.

The photoresponsivity represents the ratio of the generated photocurrent to the incident light power on the area of the PD and it is presented in Equation (1) [4–8]. Using the photocurrent value of 1.2 nA, light power density of 50 μW/cm^2 at a wavelength of 365 nm, and ZNW exposed area of 1 μm^2, the calculated photoresponsivity for the single-ZNW was found to be around 2400 A/W.

$$\mathcal{R} = I_{ph}/P_{opt}A \quad (1)$$

where P_{opt} is the light power density and A is the ZNW exposed area. As for the ZNB-based PD, the exact exposed area of the UV irradiated field is difficult to calculate due to the hierarchical complex nature of the surface. Subsequently, calculating the exact value of photoresponsivity is difficult as well. However, we

17500443, 2022, 12, Downloaded from https://ietresearch.onlinelibrary.wiley.com/doi/10.1049/nna2.12135 by Test, Wiley Online Library on [14/10/2022]. See the Terms and Conditions (https://onlinelibrary.wiley.com/terms-and-conditions) on Wiley Online Library for rules of use; OA articles are governed by the applicable Creative Commons License

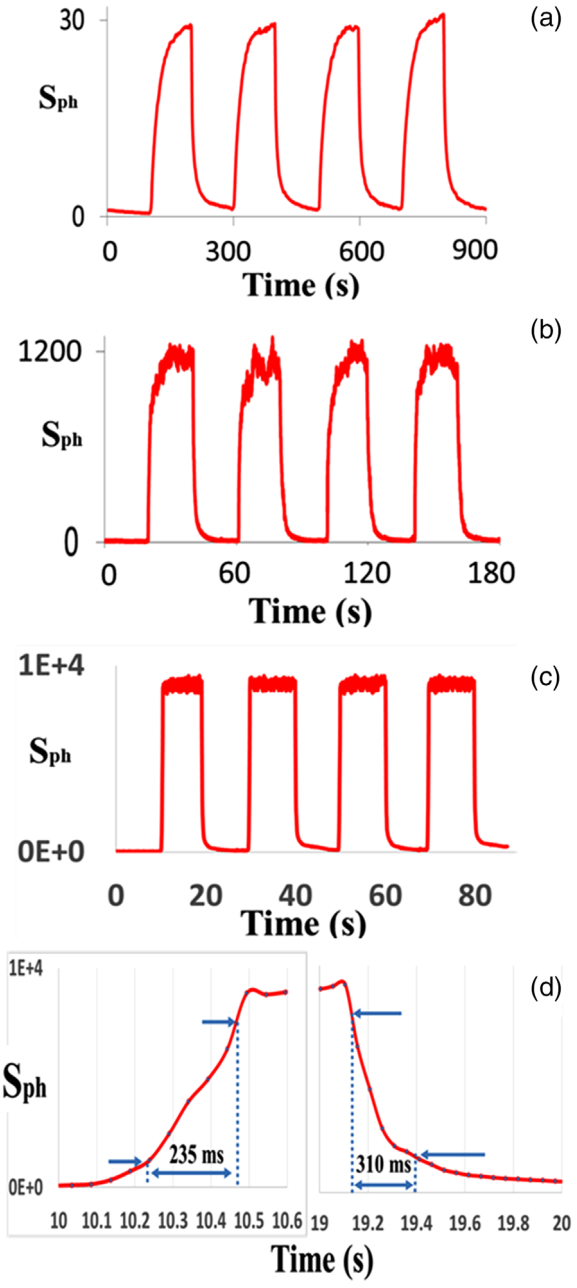


FIGURE 5 The photoresponse characteristics of the (a) ZNWA-based, (b) single ZNW-based and (c) ZNB-based PDs. (d) The corresponding response and recovery times of the ZNB-based PDs. PD, photodetector.

hypothesize it is much less than the single-ZNW photoresponsivity because the photocurrent value of the multiple-nanodisk is smaller and has a larger exposed area.

The external quantum efficiency η_{ext} represents how many carriers circulate in the detector per adsorbed photon and per unit time, and it is represented as follows [4–8]:

$$\eta_{ext} = (\tau/\tau_t) = (hc/e\lambda) \times \left(I_{ph}/P_{opt}A\right) \quad (2)$$

where τ is the hole life time and τ_t is the time needed for electrons to reach the electrodes, respectively, λ is the excitation wavelength, c is the velocity of light, h is Planck's constant, and e is the electronic charge. For the present device the record external quantum efficiency value is calculated to be 8.2×10^3. These calculated values of the photoresponsivity and external quantum efficiency are compared with those recently reported in the literature for different inorganic metal oxide nanostructure PDs in Table 1.

Figure 6 shows a comparison of the generation and transportation processes of carriers in ZNW- and ZNB-based PDs. Note that because of oxygen vacancies (V_O) in ZnO, which donate electrons to its conduction band, these materials are n-type semiconductors [23]. Therefore, in the dark and under air, the ZNWs adsorb oxygen molecules on their surfaces, and capture electrons from the conduction band to give oxygen ions (O^{2-}) and produce a low-conductivity depletion layer closer to the surface. This creates band bending because of the negative charge at the surface, which extends into the quantum confinement vertical to the ZNW surface because of quantum size properties. Therefore, a surface potential barrier is produced. Consequently, under UV irradiation, electron–hole pairs are created in the ZNWs, and holes are attracted to the negatively charged surface and become trapped

$$h\nu \rightarrow e^- + h^+ \quad (3)$$

At the surface, oxygen ions neutralise the trapped holes and increase conductivity by freeing electrons into the confined core

$$O_2^- (ad) + h^+ \rightarrow O_2 (g) \quad (4)$$

As a result, under the UV excitation the depletion layer becomes narrower, and the current gradually increases until reaction saturation. When UV irradiation of the ZNWs is stopped, electron–hole recombination occurs, resulting in oxygen molecules being re-adsorbed on the ZNW surface. Consequently, electrons are recaptured, the depletion layer is widened, and the conductivity of the ZNWs is reduced [36–38].

Crucially, the conductivity of ZNB-based PD is controlled by a mechanism which is not available in ZNW-based PD, as the former conduction channel contains nanojunctions between the initial and secondary ZNWs. As a consequence, the electrons must overcome the junction barrier so that current can flow. The formation of these barriers is by the surface depletion layers of the initial and secondary ZNWs, and so the conductance of the ZNW can be given by

$$G = n_0 e\mu\pi (R - 2t_c)/4l \quad (5)$$

where n_0 is the density of the free charge carrier, μ is the mobility of the charge carriers, R is the ZNW diameter, t_c is the surface charge region thickness, and l is the distance between the two electrodes. The thickness of the depletion region t_c is expressed as

$$t_c = L_D (eV_S/kT)^{1/2} \quad (6)$$

17500443, 2022, 12, Downloaded from https://ietresearch.onlinelibrary.wiley.com/doi/10.1049/nna2.12135 by Test, Wiley Online Library on [14/10/2022]. See the Terms and Conditions (https://onlinelibrary.wiley.com/terms-and-conditions) on Wiley Online Library for rules of use; OA articles are governed by the applicable Creative Commons License

TABLE 1 Recently reported photoresponsivity and external quantum efficiency values in comparison with the ZnO UV PDs fabricated in this work

Photodetector	$\mathcal{R}$	η_{ext}	$t_{response}$	$t_{recovery}$	Reference
ZnS nanobelt	0.12 A W^{-1} at 5 V	50%	<0.3 s	<0.3 s	[3]
Nb_2O_5 nanobelt	15.2 A W^{-1} at 1 V	6070%	–	–	[4]
Sb_2Se_3 nanowire	8.0 A W^{-1} at 5 V	1650%	<0.3 s	<0.3 s	[5]
ZnO nanoparticles	61 A W^{-1} at 120 V	–	<0.1 s	1 s	[6]
TiO_2 nanocrystals	199 A W^{-1} at 5 V	–	6 s	15 s	[7]
ZnO hollow-sphere	13.5 A W^{-1} at 5 V	–	< 5 ms	< 5 ms	[8]
ZnO nanodisk	3386 A W^{-1} at 3 V	1.2×10^4 %	15 s	65 s	[9]
p-CuZnS/n-TiO_2 nanotube array	640 A W^{-1} at 3 V	2.3×10^5 %	<0.2 s	<0.2 s	[29]
$Sr_2Nb_3O_{10}$ nanosheets	1214 A W^{-1} at 3 V	5.6×10^5 %	0.4 ms	40 ms	[30]
ZnO/NiO heterojunction arrays	0.415 mA W^{-1} at 0 V	–	7.5 s	4.8 s	[31]
ZnO nanofibre arrays homojunction	1.28 mA W^{-1} at 0 V	–	3.9 s	4.71 s	[32]
ZnO–Ga_2O_3 core–shell heterostructure microwire	9.7 mA W^{-1} at 0 V	–	0.1 ms	0.9 ms	[33]
PANI/ZnO heterojunction	0.56 mA W^{-1} at −3 V	–	0.11 ms	1.45 ms	[34]
BTO-ZnO bilayer film	1.28 mA W^{-1} at 3 V	–	0.11 ms	5.8 ms	[35]
ZnO nanowire	2400 A W^{-1} at 2 V	8.2×10^3 %	11 s	15 s	This work
ZnO nanobrush	¬	¬	235 ms	310 ms	This work

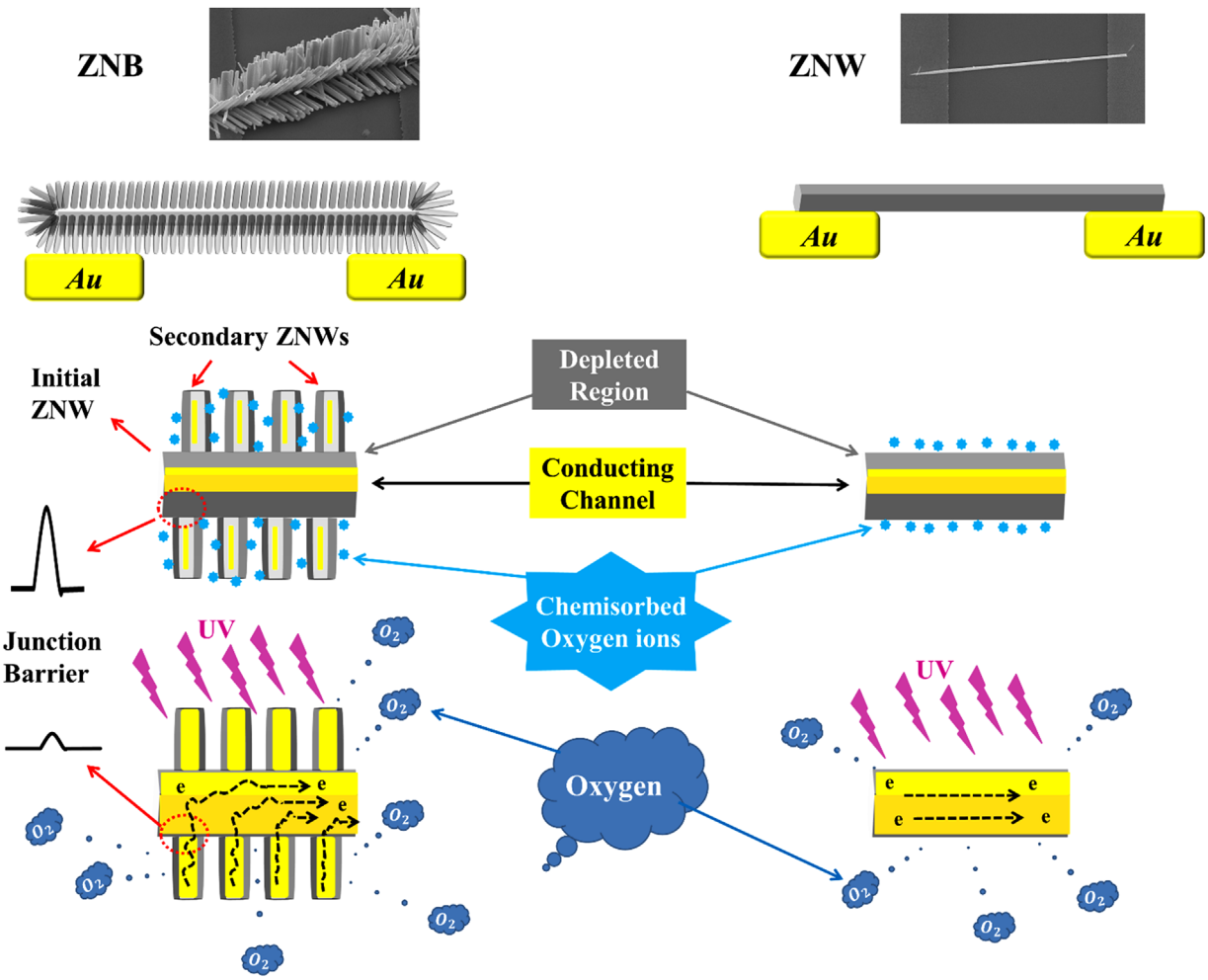


FIGURE 6 Schematic diagram showing the carrier generation and transportation process in the ZNW-based versus the ZNB-based UV PDs. UV, ultraviolet.

17500443, 2022, 12, Downloaded from https://ietresearch.onlinelibrary.wiley.com/doi/10.1049/nna2.12135 by Test, Wiley Online Library on [14/10/2022]. See the Terms and Conditions (https://onlinelibrary.wiley.com/terms-and-conditions) on Wiley Online Library for rules of use; OA articles are governed by the applicable Creative Commons License

where V_S is the adsorbate-induced band bending and L_D is the Debye length, which is expressed as

$$L_D = \left(\varepsilon\varepsilon_0 kT/e^2 n_0\right)^{1/2} \quad (7)$$

where ε is the relative dielectric permittivity of the nanomaterial [39]. Thus, the depletion regions in the initial and secondary ZNWs act as barriers to electron movement. Therefore, when the ZNW diameter exceeds the Debye length, the predominant modulator of charge transport in the ZNB-based PD is the nanojunction between the initial and secondary ZNWs.

Therefore, improvements to the response and recovery times for the ZNB-based PD are the result of controlling the charge transport by the nanojunction barrier. Depleting the conducting channel of the ZNWs by diffusing and re-adsorbing oxygen is a comparatively slow process [40, 41]; therefore, the charge recovery process is also relatively slow if the PD conductance is controlled only by the ZNW conductance, as with the SNW- and ZNWA-based PDs. However, the conductance in the ZNB-based PD is dominated by the nanojunction barriers, which are essentially two consecutive Schottky barriers. As there is an exponential association between the tunnel current across the junction barrier and the height of the barrier, the current has increased sensitivity to minor variations in the barrier. When UV irradiation ceases, electron–hole recombination occurs which increases the effective barrier because of the significant reduction in the carrier density. The dominant effects of the created junction barrier result in ultrafast current decay, and the photoinduced barrier height modulation is significantly more rapid than the oxygen diffusion process, which accounts for the better performance of the ZNB-based PD [42].

4 | CONCLUSION

We have reported upon the successful development of a cost-effective and facile hydrothermal synthesis method to produce high-performance ZnO nanostructured PDs. Being able to rationally control the morphology and structure of the produced nanomaterial was illustrated by tuning the experimental parameters used in the growth process. Crucially, the ZNB-based UV PD showed an improvement in photosensitivity (~10^4), an ultrafast response time (235 ms), and a good recovery time (310 ms) in comparison to other devices prepared using other ZnO nanomaterials. The enhanced response and recovery times reached for the ZNB-based PD were the result of distinct nanojunction barrier-dominated conductivity. In addition, the system's high photosensitivity was because of the reduction in size and the ultrahigh surface-to-volume ratio compared to the other mono-morphological nanomaterials. Thus, our observations reveal that this hydrothermal method should also extend to the low-cost and large-scale fabrication of other practical devices using various metal oxides.

DECLARATIONS

I declare that the authors have no competing interests, or other interests that might be perceived to influence the results and/or discussion reported in this paper.

CONFLICT OF INTEREST

The authors declare no conflict of interest.

DATA AVAILABILITY STATEMENT

The data that support the findings of this study are available from the corresponding author upon reasonable request.

REFERENCES

1. Ouyang, W., Chen, J., Shi, Z., Fang, X.: Self-powered UV photodetectors based on ZnO nanomaterials. Appl. Phys. Rev. 8, 031315 (2021)
2. Zhang, J., Liu, Y., Ronneberger, S., Tarakina, N.V., Merbouh, N., Loeffler, F.F.: Nanolayer laser absorber for femtoliter chemistry in polymer reactors. Adv. Mater. 34, 2108493 (2022)
3. Fang, X.; Bando, Y.; Liao, M.; Gautam, U.K.; Zhi, C.; Dierre, B.; Liu, B.; Zhai, T.; Sekiguchi, T.; Koide, Y.; Golberg, D.: Single-crystalline ZnS nanobelts as ultraviolet-light sensors. Adv. Mater. 21, 2034–2039 (2009)
4. Fang, X.; Hu, L.; Huo, K.; Gao, B.; Zhao, L.; Liao, M.; Chu, P.K.; Bando, Y.; Golberg, D.: New ultraviolet photodetector based on individual Nb_2O_5 nanobelts. Adv. Funct. Mater. 21, 3907–3915 (2011)
5. Zhai, T.Y.; Ye, M.F.; Li, H.Q.; Huang, Y.; Fang, X.S.; Liao, M.; Zhou, H.S.; Li, Y.F.; Koide, Y.; Bando, Y.; Golberg, D.: Single-crystalline Sb_2Se_3 nanowires for high-performance field-emitters and photodetectors. Adv. Mater. 22, 4530–4533 (2010)
6. Jin, Y.Z.; Wang, J.P.; Sun, B.Q.; Blakesley, J.C.; Greenham, N.C.: Solution-processed ultraviolet photodetectors based on colloidal ZnO nanoparticles. Nano Lett. 8, 1649–1653 (2008)
7. Xue, H.L.; Kong, X.Z.; Liu, Z.R.; Liu, C.X.; Zhou, J.R.; Chen, W.Y.; Ruan, S.P.; Xu, Q.: TiO_2 based metal-semiconductor-metal ultraviolet photodetectors. Appl. Phys. Lett. 90, 201118 (2007)
8. Chen, M.; Hu, L.; Xu, J.; Liao, M.; Wu, L.; Fang, X.: ZnO hollow-sphere nanofilm-based high-performance and low-cost photodetector. Small 7, 2449–2453 (2011)
9. Alenezi, M.R., Alshammari, A.S., Jayawardena, K.D.G.I., Beliatis, M.J., Henley, S.J., Silva, S.R.P.: Role of the exposed polar facets in the performance of thermally and UV activated ZnO nanostructured gas sensors. J. Phys. Chem. C 117, 17850 (2013)
10. Huang, M.H., Mao, S., Feick, H., Yan, H., Wu, Y., Kind, H., Weber, W., Russo, R., Yang, P.: Room-temperature ultraviolet nanowire nanolasers. Science 292(5523), 1897–1899 (2001)
11. Alenezi, M.R., Alshammari, A.S., Alzanki, T.H., Jarowski, P., Henley, S.J., Silva, S.R.P.: ZnO nanodisk based UV detectors with printed electrodes. Langmuir 30(13), 3913–3921 (2014)
12. Wang, R.C., Lin, H.Y., Wang, C.H., Liu, C.P.: Fabrication of a large-area Al-doped ZnO nanowire array photosensor with enhanced photoresponse by straining. Adv. Funct. Mater. 22, 3875 (2012)
13. Peng, L., Hu, L., Fang, X.: Low-dimensional nanostructure ultraviolet photodetectors. Adv. Mater. 25, 5321–5328 (2013)
14. Fang, X., Bando, Y., Liao, M., Gautam, U.K., Zhi, C., Dierre, B., Liu, B., Zhai, T., Sekiguchi, T., Koide, Y., Golberg, D.: Single-crystalline ZnS nanobelts as ultraviolet-light sensors. Adv. Mater. 21, 2034–2039 (2009)
15. Wang, Z.L.: Zinc oxide nanostructures: Growth, properties and applications. J. Phys. Condens. Matter. 16, R829 (2004)
16. Tang, Q., Zhou, W.J., Shen, J.M., Zhang, W., Kong, L.F., Qian, Y.T.: A template-free aqueous route to ZnO nanorod arrays with high optical property. Chem. Commun. 6, 712–713 (2004)
17. Li, W.J., Shi, E.W., Zhong, W.Z., Yin, Z.W.: Growth mechanism and growth habit of oxide crystals. J. Cryst. Growth. 203, 186–196 (1999)

17500443, 2022, 12, Downloaded from https://ietresearch.onlinelibrary.wiley.com/doi/10.1049/mna2.12135 by Test, Wiley Online Library on [14/10/2022]. See the Terms and Conditions (https://onlinelibrary.wiley.com/terms-and-conditions) on Wiley Online Library for rules of use; OA articles are governed by the applicable Creative Commons License

18. Liang, J.B., Liu, J.W., Xie, Q., Bai, S., Yu, W.C., Qian, Y.T.: Hydrothermal growth and optical properties of doughnut-shaped ZnO microparticles. J. Phys. Chem. B 109, 9463–9467 (2005)
19. Ni, Y.H., Wei, X.W., Ma, X., Hong, J.M.: J. Cryst. Growth. 283, 48 (2005)
20. Pal, U., Santiago, P.: Controlling the morphology of ZnO nanostructures in a low-temperature hydrothermal process. J. Phys. Chem. B 109, 15317–15321 (2005)
21. Oner, M., Norwig, J., Meyer, W.H., Wegner, G.: Control of ZnO crystallization by a PEO-*b*-PMAA diblock copolymer. Chem. Mater. 10, 460–463 (1998)
22. Li, F., Ding, Y., Gao, P., Xin, X., Wang, Z.L.: Single-crystal hexagonal disks and rings of ZnO: Low-temperature, large-scale synthesis and growth mechanism. Angew. Chem., Int. Ed. 43(39), 5238–5242 (2004)
23. Alenezi, M.R., Alzanki, T.H., Almeshal, A.M., Alshammari, A.S., Beliatis, M.J., Henley, S.J., Silva, S.R.P.: Hierarchically designed ZnO nanostructure based high performance gas sensors. RSC Adv. 4, 49521–49528 (2014)
24. Alenezi, M.R., Henley, S.J., Emerson, N.G., Silva, S.R.P.: From 1D and 2D ZnO nanostructures to 3D hierarchical structures with enhanced gas sensing properties. Nanoscale 6, 235–247 (2014)
25. Alenezi, M.R., Henley, S.J., Silva, S.R.P.: On-chip fabrication of high Performance nanostructured ZnO UV detectors. Sci. Rep. 5, 8516 (2015)
26. Alenezi, M.R.: Mater. Sci. Eng. B 236, 132 (2018)
27. Alenezi, M.R., Alzanki, T.H., Almeshal, A.M., Alshammari, A.S., Beliatis, M.J., Henley, S.J., Silva, S.R.P.: A model for the impact of the nanostructure size on its gas sensing properties. RSC Adv. 5, 103195–103202 (2015)
28. Alenezi, M.R., Almeshal, A.M.: Bridging nanowires for enhanced gas sensing properties. Crystals 11, 743 (2021)
29. Xu, X., Chen, J., Cai, S., Long, Z., Zhang, Y., Su, L., He, S., Tang, C., Liu, P., Peng, H., Fang, X.: A real-time wearable UV-radiation monitor based on a high-performance p-CuZnS/n-TiO2 photodetector. Adv. Mater. 30, 1803165 (2018)
30. Li, S., Zhang, Y., Yang, W., Liu, H., Fang, X.: 2D perovskite $Sr_2Nb_3O_{10}$ for high-performance UV photodetectors. Adv. Mater. 32, 1905443 (2020)
31. Zhang, Z., Ning, Y., Fang, X.: From nanofibers to ordered ZnO/NiO heterojunction arrays for self-powered and transparent UV photodetectors. J. Mater. Chem. C 7, 223–229 (2019)
32. Ning, Y., Zhang, Z., Teng, F., Fang, X.: Novel transparent and self-powered UV photodetector based on crossed ZnO nanofiber array homojunction. Small 14, 1703754 (2018)
33. Zhao, B., Wang, F., Chen, H., Zheng, L., Su, L., Zhao, D., Fang, X.: An ultrahigh responsivity (9.7 mAW^{-1}) self-powered solar-blind photodetector based on individual ZnO–Ga_2O_3 heterostructures. Adv. Funct. Mater. 27, 1700264(2017)
34. Chen, Y., Sua, L., Jiang, M., Fang, X.: Switch type PANI/ZnO core-shell microwire heterojunction for UV photodetection. J. Mater. Sci. Technol. 105, 259–265 (2022)
35. Zhang, Y., Zhao, X.,Chen, J., Li, S., Yang, W., Fang, X.: Self-polarized $BaTiO_3$ for greatly enhanced performance of ZnO UV photodetector by regulating the distribution of electron concentration. Adv. Funct. Mater. 30, 1907650 (2020)
36. Lin, C.C., Chen, S.Y., Cheng, S.Y., Lee, H.Y.: Properties of nitrogen-implanted *p*-type ZnO films grown on Si_3N_4/Si by radio-frequency magnetron sputtering. Appl. Phys. Lett. 84, 5040 (2004)
37. Tachikawa, T., Fujitsuka, M., Majima, T.: Mechanistic insight into the TiO_2 photocatalytic reactions: Design of new photocatalysts. J. Phys. Chem. C 111, 5259–5275 (2007)
38. Peng, L., Zhao, Q., Wang, D., Zhai, J., Wang, P., Pang, S., Xie, T.: Ultraviolet-assisted gas sensing: A potential formaldehyde detection approach at room temperature based on zinc oxide nanorods. Sens. Actuators B 136, 80 (2009)
39. Sysoev, V.V., Button, B.K., Wepsiec, K., Dmitriev, S., Kolmakov, A.: Toward the nanoscopic "electronic nose": Hydrogen vs carbon monoxide discrimination with an array of individual metal oxide nano- and mesowire sensors. Nano Lett. 6, 1584–1588 (2006)
40. Zhou, J., Gu, Y., Hu, Y., Mai, W., Yeh, P.-H., Bao, G., Sood, A.K., Polla, D.L., Wang, Z.L.: Gigantic enhancement in response and reset time of ZnO UV nanosensor by utilizing Schottky contact and surface functionalization. Appl. Phys. Lett. 94, 191103 (2009)
41. Umar, A., Kim, B.K., Kim, J.J., Hahn, Y.B.: Optical and electrical properties of ZnO nanowires grown on aluminium foil by non-catalytic thermal evaporation. Nanotechnology 18, 175606 (2007)
42. Yan, C., Singh, N., Lee, P.S.: Wide-bandgap Zn_2GeO_4 nanowire networks as efficient ultraviolet photodetectors with fast response and recovery time. Appl. Phys. Lett. 96, 053108 (2010)

How to cite this article: Alenezi, M.R., Almeshal, A.M., Alkhaledi, A.N.F.N.R.: Hierarchical zinc oxide nanobrushes ultraviolet photodetector. Micro Nano Lett. 17, 299–308 (2022). https://doi.org/10.1049/mna2.12135

17500443, 2022, 12, Downloaded from https://ietresearch.onlinelibrary.wiley.com/doi/10.1049/mna2.12135 by Test, Wiley Online Library on [14/10/2022]. See the Terms and Conditions (https://onlinelibrary.wiley.com/terms-and-conditions) on Wiley Online Library for rules of use; OA articles are governed by the applicable Creative Commons License



https://dspace.org/

Hierarchical zinc oxide nanobrushes ultraviolet photodetector

Alenezi, Mohammad R.; Almeshal, Abdullah M.; Alkhaledi, Abdullah N. F. N. R.

2022-07-12
Wiley for Institution of Engineering and Technology (IET)
https://doi.org/10.1049/mna2.12135
Alenezi MR, Almeshal AM, Alkhaledi ANFNR. (2022) Hierarchical zinc oxide nanobrushes ultraviolet photodetector. Micro and Nano Letters, Volume 17, Issue 12, 21 October 2022, pp. 299-308

Downloaded from a DSpace repository. https://dspace.org/